ARTICLE

Unravelling steady-state bulk recombination dynamics in thick efficient vacuum-deposited perovskite solar cells by transient methods

Received 00th January 20xx,
Accepted 00th January 20xx

DOI: 10.1039/x0xx00000x

David Kiermasch,[a] Lidón Gil-Escrig,[bc] Andreas Baumann,[d] Henk J. Bolink,[b] Vladimir Dyakonov*[ad] and Kristofer Tvingstedt*[a]

Accurately identifying and understanding the dominant charge carrier recombination mechanism in perovskite solar cells is of crucial importance for further improvements of this already promising photovoltaic technology. Both optical and electrical transient methods have previously been employed to strive for this warranted goal. However, electrical techniques can be strongly influenced by the capacitive response of the device which overlays with the steady-state relevant bulk carrier recombination. To ascertain the identification of bulk charge carrier dynamics, it is beneficial to evaluate thicker films to minimize the impact of device capacitance. Herein, the electrical transient response in very efficient planar co-evaporated n-i-p solar cells is studied by varying the active layer thickness from 500 nm to 820 nm and compared to a solution-processed perovskite device with an active layer of 350 nm. In case of the n-i-p devices, the capacitance for the 500 nm solar cell leads to longer perceived decay times in the lower voltage regime, while in the higher voltage regime quite similar kinetics independent of active layer thickness are observed, allowing us to identify the transition from capacitance-affected to the sought-after bulk charge carrier dynamics. We show that increasing the perovskite thickness by more than 50 % does not affect the recombination dynamics significantly, confirming the high quality of the vacuum-processed perovskite solar cells. Finally, it is demonstrated for the first time for perovskite solar cells that the recombination order in both thicker devices is ranging between 1.6 to 2, pointing towards trap-assisted and free-carrier recombination under operating conditions. We emphasize that the observed low recombination orders are in strong contrast to earlier literature as well as to the thinner solution-processed device, which suffers from both shorter carrier lifetimes and a larger device capacitance.

Introduction

Perovskite solar cells are expected to be very cost-effective as they, just like organic photovoltaics (OPV), can be easily processed via simple printing and vacuum techniques. Very low cost of module production is hence envisaged, but as for any photovoltaic technology, high power conversion efficiency (PCE) and long-term stability is paramount for making devices attractive for the energy market. The remarkable rise in PCE's for perovskite photovoltaics can mainly be attributed to a very exhaustive optimization of material combinations and deposition methods that today has enabled high crystal quality of the formed photoactive layers. The current PCE record above 24 %[1] is already very impressive, and the device film formation of these high efficiency cells is a work of art in processing optimization.

Despite the remarkable development of this photovoltaic material class, there however remains a deficiency in the overall fundamental understanding of the physics of charge carrier recombination. Further improvements in the performance can now only be reached with a raised detailed understanding of the dynamics that govern the remaining loss mechanisms. The correct assignment of the non-radiative losses and their carrier density dependence is yet to be completed. A first step towards this identification requires assigning both the correct recombination rate and order to the dominant loss process at each charge carrier density. Currently, several speculations exist,[2, 3] for example regarding a non-radiative second-order process. For this process, however, no clear physical origin is easily identified. In OPV's, similar non-radiative recombination was described and assigned to coupling to high energy vibrational modes, of which not many are needed to allow for non-radiative transitions.[4] In perovskites, such high energetic phonons do not exist[5] and justifying the existence of second order non-radiative recombination behavior becomes harder. Although lead halide perovskites are considered defect tolerant,[6] solar cells are still partially suffering from deep energy states acting like charge carrier traps and the associated recombination centers are believed to still be a prominent source of non-radiative recombination. In addition to this, the influence of imperfect charge carrier selectivity of currently

[a] Experimental Physics VI, Julius-Maximilian University of Würzburg, Am Hubland, 97074 Würzburg, Germany.
[b] Instituto de Ciencia Molecular, Universidad de Valencia, C/ J. Beltrán 2, 46980, Paterna, Spain.
[c] Current address: Helmholtz-Zentrum Berlin für Materialien und Energie GmbH, Kekuléstraße 5, 12489 Berlin, Germany.
[d] Bavarian Center for Applied Energy Research, Magdalene-Schoch-Str. 3, 97074 Würzburg, Germany.
eMail: dyakonov@physik.uni-wuerzburg.de, ktvingstedt@physik.uni-wuerzburg.de
Electronic Supplementary Information (ESI) available: [details of any supplementary information available should be included here]. See DOI: 10.1039/x0xx00000x

employed electrodes embodies a potential source of surface recombination.[7] Most efforts on recombination dynamics conducted up to now have however been focused on lifetime assignments of the pure absorber layer itself. Carrier lifetime determination in perovskite films was already conducted by contact-free techniques such as terahertz spectroscopy,[8] photoluminescence (PL) transients[2, 9-12] or transient microwave photoconductivity (TRMC)[13, 14]. More recent works have included the contribution of trap-mediated recombination in the bulk of the perovskites, leading to longer assigned lifetimes indicative of the existence of a distribution of shallow trap states.[15] This is in contrast to earlier assignments of mid-gap defect distributions which instead have the effect of speeding up recombination. Staub and coworkers later clarified the role of photon recycling effects that strongly enhances the perceived lifetime obtained from PL decay measurements.[16] Nevertheless, they were able to account for this and provided internal radiative rate constants as well as minority and majority trap-assisted Shockley-Read-Hall (SRH) lifetimes in pure perovskite films. Work on completed devices by Paulke[17] showed on the contrary that the recombination can be described by second-order free-carrier dynamics, however with the need to invoke a "time-dependent" rate constant. A clear picture on the true nature and dynamics of photogenerated charge carriers within the perovskite absorber layer, as well as on the interface towards the employed transport layers and electrodes in actual operational devices, is generally still largely missing.

Insights into recombination losses, which occur in completed devices, can be gained by studying the transient behavior of the open-circuit voltage (V_{oc}). During the past decades, transient electrical measurement techniques have been frequently employed, as these methods in principle allow to access charge carrier lifetimes, densities, recombination orders and mobilities. In earlier dye-sensitized solar cell (DSSC) and OPV evaluation, a frequently employed method to assess the dynamics of excess carrier recombination in complete devices is based on combining small-perturbation transient photovoltage[18] (TPV) with either transient photocurrent (TPC) (combined to a procedure called differential charging[19]) or charge extraction (CE).[20] (The term "excess carriers" is used to distinguish them from the equilibrium carriers that also are present in the device under dark and zero voltage conditions.) Carrier lifetime and density determination has thus already widely been used for DSSC,[21-23] OPVs[19, 20, 24] and recently also for perovskites.[25-29] First attempts of employing these methods on mesoporous perovskite devices was conducted by O´Regan[25] who emphasized the difficulties of obtaining the correct number of extracted charge carriers and the necessity to distinguish bulk and interface contribution. Electrical transient methods may therefore in principle provide very useful information of full devices, but only if conducted with care and interpreted correctly. Very recently, we outlined[30] that these methods can in fact be rather limited when it comes to correctly determining true bulk lifetimes relevant under steady-state conditions. We showed that the measured charge carrier lifetime must significantly exceed a characteristic capacitive lifetime limit set by the ratio of the device capacitance and the recombination current to at all be associated with a relevant steady-state value.[30] Recent works[25, 27, 31-34] have up until now observed a quite strong carrier lifetime dependence on the density of charge carrier concentration. These works accordingly provided kinetics in devices with recombination orders ranging between 3 and 7, by employing electrical transient methods. Reconciling such high recombination orders under steady-state operational conditions is however not straightforward. We here argue first that third-order Auger recombination is very unlikely in perovskite devices operating around sun illumination conditions, and we are more convinced that even higher order processes are tremendously more unlikely. To be able to reliably determine correct recombination orders in thin film solar cells it is accordingly imperative to reduce the factors that are known to obstruct the assignment of lifetimes and carrier densities. Kirchartz et al.[35] and Deledalle et al.[36] have previously shown for organic solar cells that the most crucial necessity to approach a correct evaluation of recombination dynamics of complete devices is to assure both high light intensities as well as thick devices. The basis of these requirements is that it is impossible to access the correct recombination order in devices where the spatial distribution of excess carriers is not homogeneous.[37] For thinner devices and lower light intensities, the gradients of excess carrier concentration inside the active layer is simply too large to allow for the assumption of one single average carrier concentration and decay rate at each evaluated intensity. However, as device thickness and light intensities are increased, the flatter does the distribution of excess charge carriers becomes, and the more justified does the assumption of $\Delta n(x)=\Delta n_{average}$ becomes.

Herein, we therefore put our efforts to assure both these requirements by evaluating thick devices under high illumination conditions. Assuring these conditions in planar devices, we believe our work possesses the uniqueness of reaching very homogeneous carrier distributions inside the active layer which allows us to for the first time also observe recombination orders which are in line with those measured in pure films, and noticeably lower than what have been observed previously in complete devices. To strengthen our argumentation, we performed reference measurements on a thinner solution-processed perovskite device, which has a larger capacitance, more inhomogeneous carrier distribution as well as shorter charge carrier lifetimes due to a larger amount of interface recombination losses at a poorly selective PEDOT:PSS interface.[38] Indeed, this solar cell does not reveal any bulk recombination parameters at all as it is universally ruled by the capacitive discharge of spatially separated charge carriers, even though measured at intensities up to 3 suns.

Results and discussion

Photovoltaic performance

Perovskite active layers can be processed either from solution[39, 40] or by (co-)evaporation[41, 42] of the constituting materials. Even though research is mostly focused on solution-based preparation techniques, the 20 % PCE limit was recently

exceeded by co-evaporation methods as well.[43, 44] To avoid the substantial changes in morphology,[45] topography[46] and surface coverage[47] observed when varying the thickness by solution-based methods, we employ the more controlled process of co-evaporation to establish uniform film thickness of 500 nm and 820 nm of methylammonium lead iodide ($MAPbI_3$). X-ray diffraction pattern of pure films is shown in Fig. S1 in the Supporting Information confirming similar crystallinity independent of thickness. Complete details on planar device preparation in the n-i-p layout can be found in the experimental section. **Fig. 1a)** shows the current-voltage (*j-V*) characteristics under simulated AM1.5G solar irradiation for the two devices with different $MAPbI_3$ layer thicknesses in forward (solid) and backward (dashed) directions. Interestingly, both kinds of solar cells show the same fill factor (FF) of 72 % and similar V_{oc}*'s* exceeding 1.1 V. The identical *FF* thus confirms that charge transport is not limiting the PCE. In contrast to several earlier publications, were an increase in perovskite thickness led to a decreased performance due to drops in V_{oc},[48] j_{sc}[45, 46] and *FF*[45, 48], we observe only an increase in j_{sc} due to increased light absorption. The 820 nm device (64 % thicker) retains a slightly higher short circuit current density leading to a higher PCE of 18.2 % compared to 17.6 % for the 500 nm solar cell. We did also not notice any changes in hysteresis upon increasing the active layer thickness as recently reported by Li et al.[49] PCE statistics on the studied solar cells (4 devices for each layer thickness) can be found in Fig. S2 in the Supporting Information. The corresponding j-V curves in the dark are presented in Fig. 1b) together with the $j_{sc}(V_{oc})$ relation[50] determined by measuring at different illumination intensities in the range of 10^{-5} up to almost 3 suns. The non-ideal Shockley equation

$$j = j_0 \cdot \left(\exp\left(\frac{qV_{oc}}{n_{id} k_b T} \right) - 1 \right) \qquad (1)$$

with the dark saturation current j_0, the elementary charge q, the thermal voltage k_bT and the ideality factor n_{id} is used to describe steady-state recombination currents in diodes (fits are represented as dashed lines). Since real devices suffer from series resistance (R_{series}) the intensity(V_{oc}) or $j_{sc}(V_{oc})$ method is more suited to provide more accurate values of n_{id}[38, 50-52] at higher voltages. Both methods however lead to quite similar values of the ideality factor in the range of 1.54 – 1.58 for the 500 nm and 1.58 – 1.60 for the 820 nm device in the voltage regime between 0.8 and 1.0 V. These values indicate that SRH recombination is present in our devices[52] and furthermore that active layer thickness does not have a significant influence on its value. Fig. 1c) shows an enlarged view of the grey rectangle in Fig. 1b). We observe an additional minor bending at voltages higher than 1.1 V. This is in line with previously observed voltage saturation effects, often seen in a multitude of solar cells when evaluated at higher intensities.[50, 53-55] Such behavior was earlier assigned to an increased recombination rate due to enhanced surface recombination,[35, 50, 56] but was very recently instead suggested to have a much simpler origin: namely device heating. Ullbrich et al. showed that just accounting for the thermal resistance of the cell is quite accurately able to explain such voltage saturation effects at higher illumination intensities.[57] This effect is not surprising in our studied samples as we approach intensities corresponding to 3 suns. The

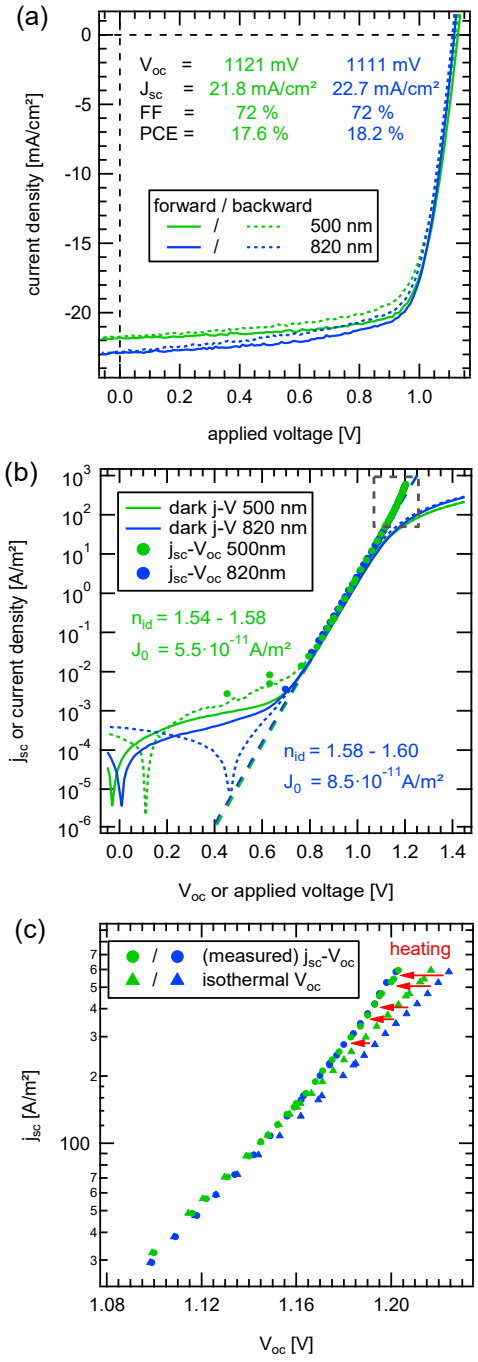

Fig. 1 Current-voltage characteristics under illumination and in the dark. (a) j-V curves for planar n-i-p devices with active layer thicknesses of 500 nm and 820 nm under AM1.5G solar irradiation. (b) Corresponding j-V characteristics in the dark (lines) including $j_{sc}(V_{oc})$ measurements for illumination intensities ranging from 10^{-5} up to 3 suns (circles). The dashed lines correspond to Shockley-fits according to equation 1. The grey rectangle is enlarged in panel (c) to demonstrate the influence of device heating on the measurements.

reduced voltages at the higher intensities can thus be explained by the fact that the heated device has an increased number of thermally generated background carriers present, forcing the V_{oc} to saturate. To demonstrate the effect of device heating we fitted the $j_{sc}(V_{oc})$ data at intermediate voltages (0.75 V - 1.00 V), where heating is negligible, to determine isothermal n_{id} and j_0. By then extrapolating this relation to higher voltages we determine the isothermal open-circuit voltage also at the higher corresponding illumination intensities/short-circuit currents (shown as triangles). The difference between the measured (heated) and the isothermal voltages reveals that the voltage saturation of the thicker, and thus more absorbing device, is slightly more pronounced and a slightly larger thermal resistance is, as expected, associated. To reduce the effect of device heating, we performed our transient electrical measurements with illumination times as short as possible but still paying attention to that a steady-state voltage has been established. As can be seen in Fig. S3 in the Supporting Information, it takes only a few hundred milliseconds for our devices to reach a stabilized V_{oc}, which is much faster compared to TiO_2-based perovskite solar cells, where times up to hundreds of seconds are sometimes needed.[58, 59] With the ambition to determine as accurately as possible how excess charge carrier density and charge carrier lifetime scales with internal voltage (and not device heating) we in the following present the measured charge carrier density and lifetime versus the determined isothermal 300 K voltages.

Relation between charge carrier density and open-circuit voltage

A true picture about the dominant recombination losses in complete solar cells can only be gained by determining the recombination order δ and the respective rate at which the charge carriers recombine at each concentration of excess charge carriers. While first-order processes ($\sim n$) via trap states are characterized by a constant lifetime, independent of charge carrier density, band-to-band free-carrier recombination shows instead a quadratic (second-order, $\sim n^2$) dependency on the density. At higher intensities the possibility of the onset of third-order Auger recombination processes must also be considered, whereas higher orders than three must certainly always be treated with greater suspicion.

To determine charge carrier density and lifetime and the corresponding dominant recombination order we used the transient techniques of CE and TPV. In general, CE can measure the excess charge carriers stored in a photovoltaic device at a fixed illumination intensity/open-circuit voltage. Further details concerning the techniques and the used setup are found in the experimental section. **Fig. 2a)** summarizes the extracted charge (normalized to the active area) of the studied devices over a plethora of open-circuit voltages measured at illumination intensities ranging from 10^{-5} suns up to almost 3 suns. Earlier publications stated that CE measurements performed on mesoporous perovskite solar cells display long extraction times in the range of tens of microseconds[60] leading to an unrealistic high amount of extracted charge,[25] which is probably caused by ion migration. In contrast, charge extraction signals obtained in this work were usually characterized by a very realistic extraction time of only a few hundred nanoseconds (Fig. S4, Supporting Information) leading also to very reasonable amount of total extracted charges. This is also in line with our previous work, where we showed that planar TiO_2-free devices do not necessarily lead to an unrealistic amount of extracted charge.[27] Unlike recent works,[25, 31, 33] we also do not note any major differences between CE and differential charging (see text and Fig. S5 in the Supporting Information). This methodological similarity can however only be obtained if capacitance corrected CE (see following text) is compared to capacitance corrected differential charging; something we believe was not the case in the recent work by Wheeler.[33] To determine the geometrical capacitance of a device and correct for the charges located at the electrodes, we performed complementary CE measurements in the dark at low negative voltages in the range from -0.35 V up to -0.05 V. The linear behavior $C = Q/U$ (Fig. S6, Supporting Information) ratifies the values for geometrical capacitance to be C_{geo} (500 nm) = 3.65 nF and C_{geo} (820 nm) = 2.88 nF confirming that the thicker perovskite layer decreases the device capacitance. The dashed lines in Fig. 2a) represent the geometrical capacitances multiplied with the studied open-circuit voltages to quantify the amount of geometric capacitive charge carriers. This amount of charge carriers thus must be subtracted from the illuminated measurements to correct for the geometrical capacitance.

The measured CE data for the illuminated case shows a clear transition into a much steeper slope at an open circuit voltage of around 1.05 V. At low voltages, both n-i-p devices demonstrate differences in the amount of total extracted charge, while it appears more similar after the 1.05 V transition. At the higher voltages the total extracted charge from the 820 nm cell however still outnumbers the amount of charge measured for the 500 nm device. The larger amount of charges in the thinner device at lower V_{oc}'s (< 1.05 V) confirms that these are indeed capacitive charge carriers located at the surfaces, while the larger amount of charges at the highest V_{oc}'s (> 1.05 V) in the thicker device (highlighted by dashed arrows) indicates instead bulk dominated volume charges. For better comparison to existing literature, we also performed CE measurements on a 350 nm thick solution-processed $MAPbI_3$-device with PEDOT:PSS as a hole transport layer and C_{60}, $PC_{60}BM$ and BCP as electron transport layers (see Supporting Information for further details and *j-V* curves in Fig. S7). In comparison to both n-i-p cells, more charges are extracted at substantially lower voltages. In addition, no transition can be observed leading to the conclusion that the extracted charge carriers are dominated by the capacitance of the device. It is here extremely important to consider that, in general, the spatial distribution of excess charge carriers in a device can be very inhomogeneous[35-37] and accordingly that the determination of excess carrier density from the measured amount of extracted charge is not at all straightforward. Only in the case of homogenous excess carrier distribution it is reasonable to divide the total extracted charge with the active layer thickness to obtain a relevant density value. As outlined in the above-mentioned works, assuring thick devices and higher illumination conditions will force the

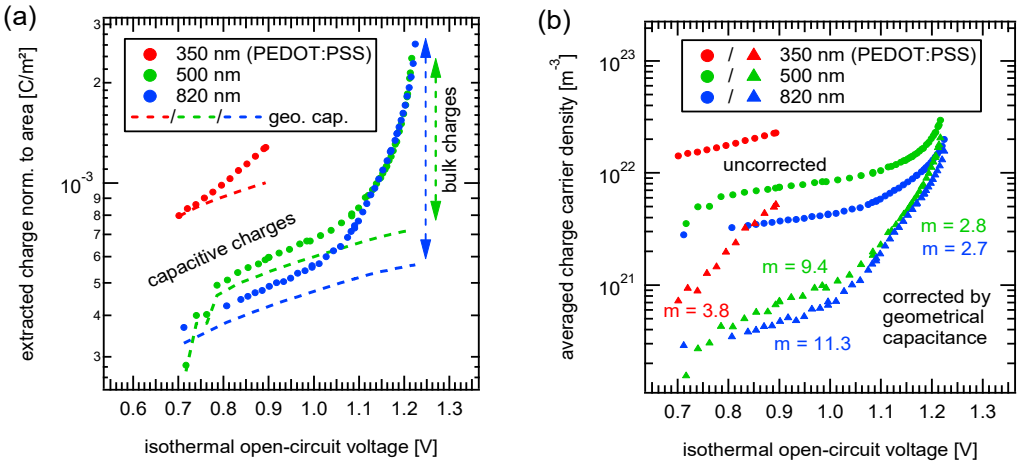

Fig. 2 Determination of charge carrier density. (a) Measured extracted charge from CE experiments plotted over the 300 K isothermal open-circuit voltages for the 500 nm and the 820 nm n-i-p and 350 nm PEDOT:PSS devices. In case of the n-i-p cells, a clear transition is visible at around 1.05 V allowing for the identification of a capacitance affected regime at low voltages and bulk-related charges at higher voltages. The PEDOT:PSS solar cell does not show a transition and displays therefore only the capacitive contribution. Dashed lines correspond to geometrical capacitance approximation from CE experiments in the dark at low negative voltages. The calculated charge carrier densities are shown in (b), where both the raw and the (capacitance) corrected data are included.

distribution of excess carriers to become more homogeneous. More importantly, the voltage dependence of inhomogeneous distributed excess carriers will be weaker than compared to evenly spatially distributed excess carriers.[35, 36] In our measured two thicker n-i-p devices, we assure these conditions and when accounting for the different volumes (Fig. 2b) we can indeed confirm that both the determined excess charge carrier densities in the bulk of the two thick devices as well as their voltage dependency are in fact quite similar, something that would not have been the case if the distribution were inhomogeneous. On the contrary, the uncorrected extracted charge carrier density of the thinner PEDOT:PSS device shows much weaker voltage dependence, signifying that this device displays a much more inhomogeneous excess carrier distribution. We note here that the capacitive-to-bulk transition observed in our thick devices occurs at voltages substantially higher compared to the PEDOT:PSS device as well as to that presented in $MAPbI_3$ devices in a recent work.[33] In addition, the corrected extracted charge in both n-i-p devices is covering more than one entire decade of excess carrier densities, far exceeding that in a majority of earlier published works, allowing us to with greater certainty also assign the important slope of the exponential relationship between voltage and excess carrier density. This relationship is usually described[35] by

$$n = n_0 \cdot e^{\frac{qV_{OC}}{mk_BT}} \qquad (2)$$

where n_0 should correspond to the equilibrium carrier density and m accounts for the deviation from the thermal voltage k_BT/q. Using this expression, we determined the m-values in both the capacitive and the bulk regime for both n-i-p devices. While the low voltage data for the n-i-p devices assigned to the capacitive regime shows (m = 9.4 for the 500 nm and m = 11.3 for the 820 nm device) very high and different m-values of no significant meaning, the relevant high voltage regime can be described by substantially lower and very similar m-values of 2.8 and 2.7 for both devices, respectively. This again points to the fact that steady-state relevant m-values shouldn't be affected by the active layer thickness, but only by the representative recombination process. The PEDOT:PSS based solar cell reveals a considerably higher m-value of 3.8. Earlier work on thickness variation[31] noted different slopes when instead altering the thickness of their transport layers (PEDOT:PSS and $PC_{70}BM$), highlighting that also these layers substantially contributes to the overall capacitance of the device, obstructing meaningful deductions of the bulk carrier density slope parameter m. In this work, we have instead assured highly conducting doped organic layers in contact with the metal electrode in combination with very thin (10 nm) undoped charge selective membranes in adjacent to the active layer. This extra added dielectric material is thus negligible with respect to the very thick perovskite film, implying minimal capacitive contribution and assuring that, at high voltages, the excess charges are indeed evenly distributed within the active layer.

Relation between charge carrier lifetime and open-circuit voltage

To determine how charge carrier lifetimes scale with the V_{oc} (and carrier density) TPV is employed for the same range of steady-state background intensities (10^{-5} - 3 suns) as for CE. TPV monitors the decay of the small photovoltage generated by a small optical perturbation light pulse on top of the steady-state open-circuit voltage defined by a continuous light source (see experimental section for further information). The induced small voltage transients are analyzed by fitting the data with a mono-exponential decay function to extract pseudo-first-order charge carrier lifetimes. In the perovskite photovoltaic literature, we note that both single[27, 32, 61-63] and double[25, 29, 63-65] exponential functions have been used to determine TPV decay times. Thereby, it appears that studies employing a double exponential fit have the presence of TiO_2 in common, while planar devices in the p-i-n layout more often show single

exponential TPV decays. This is in line with reports,[25, 29, 65] where (mesoporous) TiO_2 was proposed as the main cause of the second and slower exponential decay, also in the small perturbation regime. **Fig. 3** summarizes the measured small-perturbation TPV lifetimes for the three perovskite solar cells determined by fitting the transients with a single exponential decay. However, for high light intensities (V_{oc} ≥ 1.10 V) the transients start to reveal more of a double exponential nature (with two lifetimes τ_1 and τ_2) for the n-i-p devices (Fig. S8 in the Supporting Information displays two examples of raw TPV signals with exponential fits for a low and a high intensity/voltage regime.) The high voltage part is zoomed in the inset of Fig. 3 implying a factor of 3 to 4 difference between the observed τ_1 and τ_2 for both layer thicknesses. Since the studied devices do not contain planar nor mesoporous TiO_2 it cannot be the origin of the two measured lifetimes. Further, in the high intensity part we note that τ_1 exhibits a stronger voltage dependence compared to τ_2, which seems to be nearly constant at around 1 µs. We remind here that voltage-independent charge carrier lifetimes describe a first-order recombination process and accordingly that it is conceivable that both first- and second-order carrier lifetimes are being measured at these high voltages. Another possible explanation could be that one lifetime corresponds to the interface and the other one can be assigned to charge carriers from the bulk of the perovskite. In general, the lifetime (thus pseudo first-order) dependency on open-circuit voltage can be expressed by

$$\tau_{\Delta n} = \tau_0 \cdot e^{-\frac{qV_{OC}}{\vartheta kT}} \qquad (3)$$

where τ_0 is the intercept at 0 V and should correspond to the equilibrium charge carrier lifetime and the factor θ accounts again for slope deviations from the thermal voltage k_BT/q. In line with the voltage dependency of charge carrier density, the small-perturbation lifetimes also show a clear transition at around 1.05 V, where the slopes for both devices changes substantially. We emphasize that this transition in the relation between charge carrier lifetime and V_{oc} has, to the best of our knowledge, previously not been identified in perovskite solar cells. For the 500 nm device, θ is determined to be 1.6 in the low voltage and 2.4 in the high voltage regime. Quite similar values are obtained for the 820 nm device where θ equals 1.7 at voltages below and 2.5 for the voltage range above 1.05 V. However, and in agreement with previous reports, the PEDOT:PSS device does not show any slope alterations over the studied open-circuit voltage range and reveals θ to be 1.4. At 1 sun illumination conditions, the PEDOT:PSS cell shows a charge carrier lifetime of about 400 ns, while both thicker n-i-p devices demonstrate a lifetime of around 800 ns. It is however unphysical, that the huge difference in open-circuit voltage of these devices could be caused by such a small discrepancy in charge carrier lifetime. For equal bulk carrier concentrations, an increase of a first-order carrier lifetime by a factor of 2 would merely lead to an increase of voltage by 18 mV (kT ln2) at room temperature, a factor of 13 less than observed. This fact solidifies that the measured lifetimes cannot be related to bulk carriers at the same time but that the PEDOT:PSS cell displays kinetics associated with a capacitive discharge instead. In line with Streets[66] earlier note, we derived[30] a condition under which relevant bulk lifetimes τ_{bulk} are accessible by these methods:

$$\tau_{bulk} >> \tau_{cap} = \frac{n_{id}k_bT}{q} \cdot \frac{C}{j_0} \cdot e^{\frac{qV_{OC}}{n_{id}kT}} = \frac{n_{id}k_bTC}{q \cdot J_{SC}(V_{OC})} \qquad . (4)$$

The bulk lifetime has therefore to exceed this characteristic time, which is entirely caused by the relaxation of spatially separated charge carriers. The fact that this discharging process can be slower than the relevant bulk processes is hence what makes it difficult to assign the steady-state relevant charge carrier lifetimes correctly. As recently pointed out by Du et al., TPV decay times can also be prolonged by the storage and release of charge carriers from shallow trap states.[34] To distinguish between bulk recombination lifetimes and capacitive discharging rate, we therefore calculated the characteristic time τ_{cap} according to equation 4 using the ideality factor n_{id} and the $j_{sc}(V_{oc})$ relation from Fig. 1b) and the geometrical capacitance C_{geo} determined by CE measurements without illumination (see Fig. 2a and S6). These values are drawn as dashed lines in Fig. 3. The following can therefore be concluded for both n-i-p devices: at low voltages (V_{oc} < 1.05 V) the measured TPV lifetime is ruled by the time it takes for charge carriers located at the respective majority carrier electrode or interface to the electrodes to find its counterpart at the other end of the device. The lifetime is accordingly well described as a capacitor that is emptied via the diode itself.[38] For voltages above 1.05 V, the charge carriers gets more evenly distributed and the measured lifetimes clearly exceed the limit of equation 4, allowing for the identification of bulk carrier

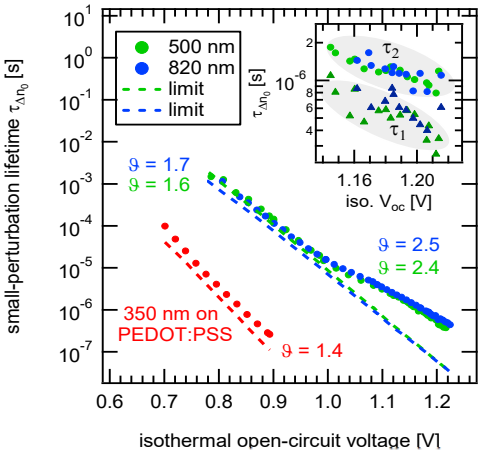

Fig. 3 Determination of charge carrier lifetimes. Small-perturbation charge carrier decay times determined by TPV for the 350 nm PEDOT:PSS and the 500 nm and 820 nm n-i-p devices. The data has been analyzed with single exponential fits. For the highest intensities, double exponential decays have been observed in both n-i-p devices as shown in the inset, where τ_1 and τ_2 times are plotted. Dashed lines correspond to the characteristic time limit (equation 4) resulting from discharging of charges at the electrodes. This limit must be exceeded to make statements about bulk relevant lifetimes, which is the case for voltages higher than 1.05 V.

lifetimes. For the highest intensities, the difference between the theoretical capacitive limit and the measured lifetimes is more than one order of magnitude. In case of the thinner PEDOT:PSS device, no clear difference between the calculated capacitive limit and the measured decay times can be observed clearly proving that these lifetimes are not real bulk carrier lifetimes. Even at the highest illumination intensities, the capacitive discharge is still longer than the bulk carrier lifetimes, which are usually in the range of a few ns in PEDOT:PSS based devices, since these cells suffer more from surface/interface recombination.[38] The small difference between the calculated and measured lifetimes for the PEDOT:PSS device can be explained by the fact that the measured lifetimes do not have their origin in a pure geometric discharge but are rather a combination of voltage independent (geometric) and voltage dependent (for example depletion layer) capacitance.

Charge carrier dynamics and recombination order

Performing TPV and CE at the same illumination intensities and thus open-circuit voltages allows us to correlate the measured lifetimes with a corresponding charge carrier density as displayed in **Fig. 4**a for the PEDOT:PSS based device and Fig. 4b for both n-i-p devices. The dashed lines correspond to the capacitive lifetime limit according to equation 4 but now plotted versus the charge carrier density instead of voltage. While the PEDOT:PSS solar cell has a constant slope and is completely limited by capacitive discharge, both n-i-p devices show the transition from a steeper slope below $1 \cdot 10^{21}$ m^{-3} to a flatter slope at high charge carrier densities. At low carrier concentrations (grey region), the decay times are longer for the 500 nm device at a fixed charge carrier density. This behavior is expected since these decay times originate from a device with a larger capacitance (and the discharging time of a capacitor is directly proportional to its capacitance) and thus confirms our statements made so far. In contrast, the lifetime-density correlation is quite similar for both devices at the higher carrier densities meaning that both devices reveal essentially very similar bulk carrier recombination dynamics. We also note, that the capacitance-to-bulk transition can be already observed at slightly lower carrier densities for the thicker device, which can be explained by the reduced impact of capacitive charge carriers on the charge carrier dynamics. In addition, τ_2 is included in Fig. 4b, showing an almost constant lifetime-density relationship pointing towards contribution from a pure first-order recombination process. Combining equations 2 and 3, the relationship between pseudo first-order carrier lifetime and carrier density can be described by the power law expression

$$\tau_{\Delta n} = \tau_0 \left(\frac{n}{n_0} \right)^{-\lambda} \qquad (5)$$

where the ratio m/ϑ is now abbreviated with λ. The parameter λ, describing the slope of the power law, represents the recombination order via the relation $\delta = \lambda + 1$.[19, 67] Values for δ are provided in Fig. 4, revealing a high recombination order of 3.8 for the PEDOT:PSS sample, in line with values presented in earlier works.[27, 31-34] In case of the n-i-p devices, even higher values of 6-7 for the 500 nm and 8-9 for the 820 nm perovskite thicknesses are obtained for densities below $1 \cdot 10^{21}$ m^{-3}, but without any physical meaning as they originate from the capacitive regime. However, for charge carrier densities above $1 \cdot 10^{21}$ m^{-3}, quite similar orders in the range of 1.7-2.0 (500 nm) and 1.6-2.0 (820 nm) can be determined. Whereas most of the earlier publications on both perovskite and organic solar cells have commonly observed noticeably higher recombination orders, the results presented on our thicker n-i-p devices are the first to observe recombination orders lower than or around 2 when determined by electrical means on completed perovskite solar cells. These determined values of recombination order are

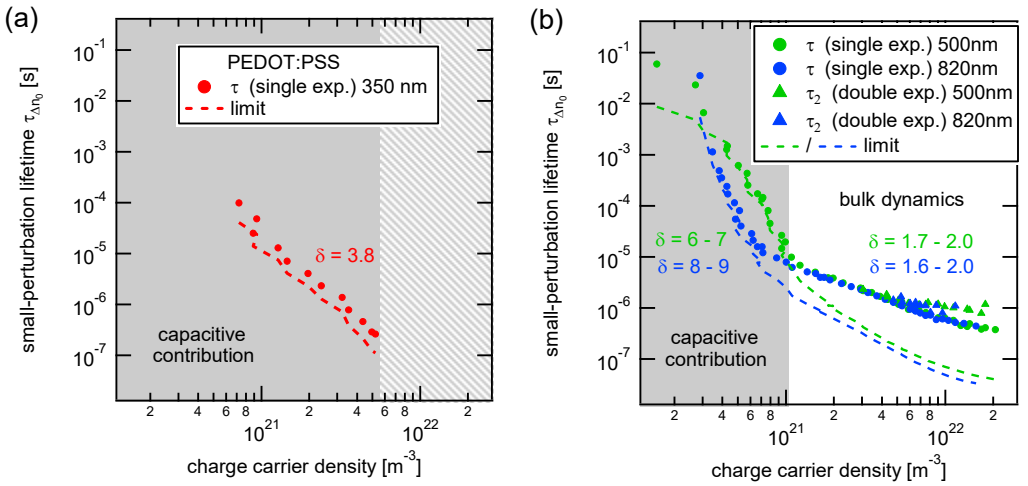

Fig. 4 Recombination dynamics for the (a) PEDOT:PSS based and the (b) two thicker 500 nm and 820 nm perovskite solar cells. The PEDOT:PSS solar cell is completey ruled by capacitive charge carriers and shows a constant slope of δ = 3.8. In case of the other devices, at $1 \cdot 10^{21}$ m^{-3}, a transition between capacitance and bulk related dynamics can be observed. While the capacitive parts show a longer lifetime for the thinner 500 nm device at a fixed carrier concentration, the bulk regimes are quite similar. In addition, the capacitive parts obey unphysically high recombination orders, while the bulk related dynamics point towards first- and second-order processes.

also more in line with literature where transient photoconductivity and photoluminescence revealed similar values in neat $MAPbI_3$ films (not integrated in a device architecture) at similar charge carrier densities around ~10^{22} m^{-3}.[68-70]

Relation of transient parameters to steady-state parameters

Transient electrical techniques can be used not only to determine charge carrier lifetimes and densities but also steady-state parameters like the ideality factor n_{id}.[71] The diode ideality factor is linked to the determined experimental parameters m and ϑ via

$$\frac{1}{n_{id}} = \frac{1}{m} + \frac{1}{\vartheta} \quad . \qquad (6)$$

By combining equation 6 with the relation $\delta = (m/\vartheta) + 1$, the recombination order can thus always also be determined[35] from

$$\delta = \frac{m}{n_{id}} \quad . \qquad (7)$$

This clarifies that the recombination order is in principle also accessible by determining merely the voltage dependence of charge carrier density and the steady state parameter n_{id}. Both equations 6 and 7 are therefore of general importance for our contribution, since they link steady-state and transient recombination parameters with each other and provide an alternative route to Fig. 4 for the determination of the recombination order δ. However, a prerequisite for this to work is again that the excess charge carriers are homogeneously distributed. A few rules of thumbs are useful to bear in mind with respect to the above equations; if the steady-state ideality factor n_{id} equals the charge carrier density slope m, then the dynamics must be first-order (δ = 1). If on the other hand the lifetime slope ϑ instead equals the density slope m, we have pure second-order recombination (δ = 2). The latter is for example the case for a solar cell operating in the radiative limit with pure band-to-band recombination. Then m and ϑ are not only equal but must also have the value 2, which will always render an ideality factor n_{id} of unity. However, these clear cases are often not observed in real thin-film solar cells.

Table 1 summarizes the measured and calculated recombination parameters determined in this work. For the n-i-p devices, the values are separated into parameters determined in the capacitive, and the relevant bulk regime, as discussed for Fig. 2, 3 and 4. Using equation 6, four calculated values for the n_{id} are thus provided and compared to the measured steady-state $j_{sc}(V_{oc})$ values. Depending on in which regime the n_{id} has been determined, the values are close or slightly underestimated compared to the steady-state value. We note that the ideality factor determined in the higher voltage regime, which we assigned to the reliable bulk values, still might be limited by a minor contribution from capacitive effects. The underestimation in n_{id} is also observed for the PEDOT:PSS based device (equation 6 leads to 1.02, while the dark *j-V* in Fig. S7 revealed 1.2), which is purely ruled by capacitance. The recombination order δ was subsequently also calculated in the two possible ways: first, by using the slopes in Fig. 4 (relying only on TPV and CE) and second, taking equation 7 with *m*-values from CE and idealities from steady-state experiments (Fig. 1b). Both methods demonstrate that parameters determined in the capacitive regime yield completely unrealistic values for δ, while representative as well as realistic orders (1.6 – 2.0) can be obtained only in the higher voltage regime for the 500 nm and 820 nm n-i-p devices, justifying our focus on the separation of the measured transient data into these two regimes. The deduced recombination order in the relevant carrier density regime thus largely rules out the occurrence of Auger effects and confirms that also devices are mostly ruled by first- and second-order dynamics independent of active layer thickness. At 1 sun illumination conditions, we identify a steady-state excess charge carrier concentration of ~$7 \cdot 10^{21}$ m^{-3} and emphasize that this is a value of carrier concentration that non-electrical methods such as TRPL, TA, THz spectroscopy and TRMC should always strive for and include in efforts of determining perovskite PV relevant decay kinetics. Our work thus constitutes a contribution to the enduring discussion[30, 35] of the correct analysis of electrical transient data, where long lifetimes and high recombination orders are sometimes observed for low carrier concentrations/illumination intensities in different solar cells technologies, possibly originating from measurements performed in the capacitance limited region. On the other hand, we clearly show that transient electrical techniques can be used to determine reliable recombination parameters in fully working perovskite devices under operating conditions if both thick active layers and high illumination conditions are ensured. In line with the *j-V* characteristics in Fig. 1a, we can conclude from our transient opto-electrical analysis that the additional 320 nm perovskite layer in this device configuration does not affect the recombination dynamics negatively, which is remarkable compared to existing literature.[31, 45, 48]

Table 1. Recombination parameters determined by steady-state (*j-V* characteristics and $j_{sc}(V_{oc})$) and transient (TPV and CE) techniques. Error margins are obtained from the fitting procedure and calculated according to uncertainty propagation.

	350 nm	500 nm		820 nm	
region	capacitive	capacitive	bulk	capacitive	bulk
m (Fig. 2b)	3.8 ± 0.2	9.4 ± 0.4	2.8 ± 0.1	11.3 ± 0.8	2.7 ± 0.1
ϑ (Fig. 3)	1.4 ± 0.1	1.6 ± 0.1	2.4 ± 0.1	1.7 ± 0.1	2.5 ± 0.1
n_{id} (transient, equation 6)	1.02 ± 0.06	1.37 ± 0.07	1.29 ± 0.04	1.48 ± 0.08	1.30 ± 0.04
n_{id} (steady-state, Fig. 1b and S7)	1.2 ± 0.1	1.54 – 1.58		1.58 - 1.60	
δ (Fig. 4)	3.8 ± 0.2	≈ 6 - 7	≈ 1.7 – 2.0	≈ 8 - 9	≈ 1.6 - 2.0
δ (equation 7, steady-state n_{id})	3.2 ± 0.3	≈ 6	≈ 1.8	≈ 7	≈ 1.7

Conclusions

In conclusion, we demonstrated that highly efficient planar perovskite devices can be manufactured with active layer thickness exceeding 800 nm without any noticeable losses in efficiency. Furthermore, accounting for the increase of equilibrium charge carrier density, originating from the induced temperature rise at the required higher intensities, we provide steady-state relevant charge carrier concentrations and lifetimes versus isothermal voltages. We showed that while it was not possible to extract useful bulk recombination parameters from the PEDOT:PSS device due to short lifetimes and high device capacitance, we identified a capacitance-to-bulk transition in the studied n-i-p perovskite photovoltaic devices. With these thick and well performing solar cells and by measuring in the high intensity regime up to 3 suns it is possible to generate homogeneously distributed excess carrier concentrations which allows us to obtain accurate and meaningful values of charge carrier densities and lifetimes in complete devices. Having eliminated the influence of spatially separated carriers, the obtained densities, lifetimes and the associated recombination order are for the first time thus also more in line with reported values on perovskite films, as determined by optical contact-less transient methods. We find that bulk recombination dynamics are not depending on perovskite thickness in accordance with the very similar open-circuit voltages (charge carrier densities) in thicker co-evaporated devices. This works therefore demonstrates that transient electrical techniques can, if correct bulk dynamics are identified, help to understand recombination losses in solar cells that will allow future opportunities on how to also suppress them.

Conflicts of interest

There are no conflicts to declare.

Acknowledgements

The work was supported by the German Research Foundation (DFG) through project 382633022 (RECOLPER) and the German Federal Ministry for Education and Research (BMBF) through the grant 03SF0514A/B (HYPER). V.D. further acknowledges the Bavarian State Ministry of Education and Culture, Science and Arts for funding of the Collaborative Research Network “Solar Technologies go Hybrid”. A.B.’s works at the ZAE Bayern is financed by the Bavarian Ministry of Economic Affairs and Media, Energy and Technology. L.G.E. and H.J.B. acknowledge financial support from the Spanish Ministry of Science, Innovation and Universities via the Unidad de Excelencia María de Maeztu MDM-2015-0538, MAT2017-88821-R, PCIN-2015-255 and PCIN-2017-014. K.T., D.K., A.B., H.J.B., and V.D. designed the study which D.K. and L.G.E. implemented experimentally. L.G.E. manufactured the devices in Valencia which D.K. measured in Würzburg. D.K. analyzed the data. D.K. and K.T. wrote the paper to which all authors contributed with feedback and comments. K.T., V.D., and H.B. supervised the project.

Notes and references

1. National Renewable Energy Laboratory, https://www.nrel.gov/pv/cell-efficiency.html (accessed May 2019).
2. F. Staub, T. Kirchartz, K. Bittkau and U. Rau, *J. Phys. Chem. Lett.*, 2017, **8**, 5084-5090.
3. J. M. Richter, M. Abdi-Jalebi, A. Sadhanala, M. Tabachnyk, J. P. H. Rivett, L. M. Pazos-Outón, K. C. Gödel, M. Price, F. Deschler and R. H. Friend, *Nat. Commun.*, 2016, **7**, 13941.
4. J. Benduhn, K. Tvingstedt, F. Piersimoni, S. Ullbrich, Y. Fan, M. Tropiano, K. A. McGarry, O. Zeika, M. K. Riede, C. J. Douglas, S. Barlow, S. R. Marder, D. Neher, D. Spoltore and K. Vandewal, *Nat. Energy*, 2017, **2**, 17053.
5. T. Kirchartz, T. Markvart, U. Rau and D. A. Egger, *J. Phys. Chem. Lett.*, 2018, **9**, 939-946.
6. K. X. Steirer, P. Schulz, G. Teeter, V. Stevanovic, M. Yang, K. Zhu and J. J. Berry, *ACS Energy Lett.*, 2016, **1**, 360-366.
7. M. Stolterfoht, P. Caprioglio, C. M. Wolff, J. A. Márquez, J. Nordmann, S. Zhang, D. Rothhart, U. Hörmann, A. Redinger, L. Kegelmann, S. Albrecht, T. Kirchartz, M. Saliba, T. Unold and D. Neher, *arXiv preprint* 2018, arXiv:1810.01333.
8. M. B. Johnston and L. M. Herz, *Acc. Chem. Res.*, 2016, **49**, 146-154.
9. Y. Yamada, T. Nakamura, M. Endo, A. Wakamiya and Y. Kanemitsu, *J. Am. Chem. Soc.*, 2014, **136**, 11610-11613.
10. R. L. Milot, G. E. Eperon, H. J. Snaith, M. B. Johnston and L. M. Herz, *Adv. Func. Mater.*, 2015, **25**, 6218-6227.
11. C. M. Wolff, F. Zu, A. Paulke, L. P. Toro, N. Koch and D. Neher, *Adv. Mater.*, 2017, **29**, 1700159.
12. L. G. Kudriashova, D. Kiermasch, P. Rieder, M. Campbell, K. Tvingstedt, A. Baumann, G. V. Astakhov and V. Dyakonov, *J. Phys. Chem. Lett.*, 2017, **8**, 4698-4703.
13. Y. Bi, E. M. Hutter, Y. Fang, Q. Dong, J. Huang and T. J. Savenije, *J. Phys. Chem. Lett.*, 2016, **7**, 923-928.
14. E. M. Hutter, G. E. Eperon, S. D. Stranks and T. J. Savenije, *J. Phys. Chem. Lett.*, 2015, **6**, 3082-3090.
15. T. Leijtens, G. E. Eperon, A. J. Barker, G. Grancini, W. Zhang, J. M. Ball, A. R. S. Kandada, H. J. Snaith and A. Petrozza, *Energy Environ. Sci.*, 2016, **9**, 3472-3481.
16. F. Staub, H. Hempel, J.-C. Hebig, J. Mock, U. W. Paetzold, U. Rau, T. Unold and T. Kirchartz, *Phys. Rev. Appl.*, 2016, **6**, 044017.
17. A. Paulke, S. D. Stranks, J. Kniepert, J. Kurpiers, C. M. Wolff, N. Schon, H. J. Snaith, T. J. K. Brenner and D. Neher, *Appl. Phys. Lett.*, 2016, **108**, 113505.
18. A. Maurano, C. C. Shuttle, R. Hamilton, A. M. Ballantyne, J. Nelson, W. M. Zhang, M. Heeney and J. R. Durrant, *J. Phys. Chem. C*, 2011, **115**, 5947-5957.
19. C. G. Shuttle, B. O’Regan, A. M. Ballantyne, J. Nelson, D. D. C. Bradley, J. de Mello and J. R. Durrant, *Appl. Phys. Lett.*, 2008, **92**, 093311.
20. A. Förtig, J. Kniepert, M. Gluecker, T. Brenner, V. Dyakonov, D. Neher and C. Deibel, *Adv. Func. Mater.*, 2014, **24**, 1306-1311.
21. N. W. Duffy, L. M. Peter, R. M. G. Rajapakse and K. G. U. Wijayantha, *J. Phys. Chem. B*, 2000, **104**, 8916-8919.

22. B. C. O'Regan and F. Lenzmann, *J. Phys. Chem. B*, 2004, **108**, 4342-4350.
23. P. R. F. Barnes, K. Miettunen, X. Li, A. Y. Anderson, T. Bessho, M. Gratzel and B. C. O'Regan, *Adv. Mater.*, 2013, **25**, 1881-1922.
24. C. G. Shuttle, A. Maurano, R. Hamilton, B. O'Regan, J. C. de Mello and J. R. Durrant, *Appl. Phys. Lett.*, 2008, **93**, 183501.
25. B. C. O'Regan, P. R. F. Barnes, X. Li, C. Law, E. Palomares and J. M. Marin-Beloqui, *J. Am. Chem. Soc.*, 2015, **137**, 5087-5099.
26. V. Roiati, S. Colella, G. Lerario, L. De Marco, A. Rizzo, A. Listorti and G. Gigli, *Energy Environ. Sci.*, 2014, **7**, 1889-1894.
27. D. Kiermasch, P. Rieder, K. Tvingstedt, A. Baumann and V. Dyakonov, *Sci. Rep.*, 2016, **6**, 39333.
28. A. Baumann, K. Tvingstedt, M. C. Heiber, S. Väth, C. Momblona, H. J. Bolink and V. Dyakonov, *APL Mater.*, 2014, **2**, 081501.
29. N. F. Montcada, J. M. Marín-Beloqui, W. Cambarau, J. Jiménez-López, L. Cabau, K. T. Cho, M. K. Nazeeruddin and E. Palomares, *ACS Energy Lett.*, 2017, **2**, 182-187.
30. D. Kiermasch, A. Baumann, M. Fischer, V. Dyakonov and K. Tvingstedt, *Energy Environ. Sci.*, 2018, **11**, 629-640.
31. I. Gelmetti, L. Cabau, N. F. Montcada and E. Palomares, *ACS Appl. Mater. Interfaces*, 2017, **9**, 21599-21605.
32. J. Jiménez-López, W. Cambarau, L. Cabau and E. Palomares, *Sci. Rep.*, 2017, **7**, 6101.
33. S. Wheeler, D. Bryant, J. Troughton, T. Kirchartz, T. Watson, J. Nelson and J. R. Durrant, *J. Phys. Chem. C*, 2017, **121**, 13496-13506.
34. T. Du, J. Kim, J. Ngiam, S. Xu, P. R. Barnes, J. R. Durrant and M. A. McLachlan, *Adv. Func. Mater.*, 2018, **28**, 1801808.
35. T. Kirchartz and J. Nelson, *Phys. Rev. B*, 2012, **86**, 165201.
36. F. Deledalle, P. Shakya Tuladhar, J. Nelson, J. R. Durrant and T. Kirchartz, *J. Phys. Chem. C*, 2014, **118**, 8837-8842.
37. C. Deibel, A. Wagenpfahl and V. Dyakonov, *Phys. Rev. B*, 2009, **80**, 075203.
38. K. Tvingstedt, L. Gil-Escrig, C. Momblona, P. Rieder, D. Kiermasch, M. Sessolo, A. Baumann, H. J. Bolink and V. Dyakonov, *ACS Energy Lett.*, 2017, **2**, 424-430.
39. M. M. Lee, J. Teuscher, T. Miyasaka, T. N. Murakami and H. J. Snaith, *Science*, 2012, **338**, 643-647.
40. J. Burschka, N. Pellet, S.-J. Moon, R. Humphry-Baker, P. Gao, M. K. Nazeeruddin and M. Gratzel, *Nature*, 2013, **499**, 316-319.
41. M. Liu, M. B. Johnston and H. J. Snaith, *Nature*, 2013, **501**, 395-398.
42. O. Malinkiewicz, A. Yella, Y. H. Lee, G. M. Espallargas, M. Graetzel, M. K. Nazeeruddin and H. J. Bolink, *Nat. Photon.*, 2014, **8**, 128-132.
43. C. Momblona, L. Gil-Escrig, E. Bandiello, E. M. Hutter, M. Sessolo, K. Lederer, J. Blochwitz-Nimoth and H. J. Bolink, *Energy Environ. Sci.*, 2016, **9**, 3456-3463.
44. D. Pérez-del-Rey, P. P. Boix, M. Sessolo, A. Hadipour and H. J. Bolink, *J. Phys. Chem. Lett.*, 2018, **9**, 1041-1046.
45. D. Liu, M. K. Gangishetty and T. L. Kelly, *J. Mater. Chem. A*, 2014, **2**, 19873-19881.
46. K. Wang, C. Liu, P. Du, L. Chen, J. Zhu, A. Karim and X. Gong, *Org. Electron.*, 2015, **21**, 19-26.
47. G. E. Eperon, V. M. Burlakov, P. Docampo, A. Goriely and H. J. Snaith, *Adv. Func. Mater.*, 2014, **24**, 151-157.
48. C. Momblona, O. Malinkiewicz, C. Roldán-Carmona, A. Soriano, L. Gil-Escrig, E. Bandiello, M. Scheepers, E. Edri and H. J. Bolink, *APL Mater.*, 2014, **2**, 081504.
49. X. Li, Y. Wang, M. Tai, X. Zhao, Y. Gu, J. Han, H. Shen, J. Li and H. Lin, *Phys. Chem. Chem. Phys.*, 2018, **20**, 16285-16293.
50. K. Tvingstedt and C. Deibel, *Adv. Energy Mater.*, 2016, **6**, 1502230.
51. M. Wolf and H. Rauschenbach, *Adv. Energy Conver.*, 1963, **3**, 455-479.
52. W. Tress, M. Yavari, K. Domanski, P. Yadav, B. Niesen, J. P. Correa Baena, A. Hagfeldt and M. Graetzel, *Energy Environ. Sci.*, 2018, **11**, 151-165.
53. S. Glunz, J. Nekarda, H. Mäckel and A. Cuevas, *2nd European Photovoltaic Solar Energy Conference and Exhibition*, 2007, 849-853.
54. O. Gunawan, T. Gokmen and D. B. Mitzi, *J. Appl. Phys*, 2014, **116**, 084504.
55. C. Law, L. Miseikis, S. Dimitrov, P. Shakya-Tuladhar, X. Li, P. R. F. Barnes, J. Durrant and B. C. O'Regan, *Adv. Mater.*, 2014, **26**, 6268-6273.
56. T. Kirchartz, F. Deledalle, P. S. Tuladhar, J. R. Durrant and J. Nelson, *J. Phys. Chem. Lett.*, 2013, **4**, 2371-2376.
57. S. Ullbrich, A. Fischer, Z. Tang, J. Ávila, H. J. Bolink, S. Reineke and K. Vandewal, *Phys. Rev. Appl.*, 2018, **9**, 051003.
58. Y. Wu, H. Shen, D. Walter, D. Jacobs, T. Duong, J. Peng, L. Jiang, Y. B. Cheng and K. Weber, *Adv. Func. Mater.*, 2016, **26**, 6807-6813.
59. D. W. deQuilettes, W. Zhang, V. M. Burlakov, D. J. Graham, T. Leijtens, A. Osherov, V. Bulović, H. J. Snaith, D. S. Ginger and S. D. Stranks, *Nat. Commun.*, 2016, **7**, 11683.
60. N. F. Montcada, M. Mendez, K. T. Cho, M. K. Nazeeruddin and E. Palomares, *Nanoscale*, 2018, **10**, 6155-6158.
61. Q. Dong, Y. Fang, Y. Shao, P. Mulligan, J. Qiu, L. Cao and J. Huang, *Science*, 2015, **347**, 967-970.
62. J.-H. Im, H.-S. Kim and N.-G. Park, *Apl Mater.*, 2014, **2**, 081510.
63. P. Calado, A. M. Telford, D. Bryant, X. Li, J. Nelson, B. C. O'Regan and P. R. F. Barnes, *Nat. Commun.*, 2016, **7**, 13831.
64. R. S. Sanchez, V. Gonzalez-Pedro, J.-W. Lee, N.-G. Park, Y. S. Kang, I. Mora-Sero and J. Bisquert, *J. Phys. Chem. Lett.*, 2014, **5**, 2357-2363.
65. J.-W. Lee, T.-Y. Lee, P. J. Yoo, M. Gratzel, S. Mhaisalkar and N.-G. Park, *J. Mater. Chem. A*, 2014, **2**, 9251-9259.
66. R. A. Street, *Phys. Rev. B*, 2011, **84**, 075208.
67. A. Foertig, A. Baumann, D. Rauh, V. Dyakonov and C. Deibel, *Appl. Phys. Lett.*, 2009, **95**, 052104.
68. S. Colella, M. Mazzeo, A. Rizzo, G. Gigli and A. Listorti, *J. Phys. Chem. Lett.*, 2016, **7**, 4322-4334.
69. C. Wehrenfennig, G. E. Eperon, M. B. Johnston, H. J. Snaith and L. M. Herz, *Adv. Mater.*, 2014, **26**, 1584-1589.
70. J. M. Richter, M. Abdi-Jalebi, A. Sadhanala, M. Tabachnyk, J. P. H. Rivett, L. M. Pazos-Outon, K. C. Godel, M. Price, F. Deschler and R. H. Friend, *Nat. Commun.*, 2016, **7**.
71. A. Förtig, J. Rauh, V. Dyakonov and C. Deibel, *Phys. Rev. B*, 2012, **86**, 115302.